Arch. Metall. Mater. **70** (2025), 2, 851-867

DOI: https://doi.org/10.24425/amm.2025.153487

S.CH. KUNDURTI[1], A. SHARMA[1*]

ENHANCING MECHANICAL, THERMAL, AND TRIBOLOGICAL PROPERTIES OF AA7075 SURFACE COMPOSITE WITH rGO-MWCNT HYBRID REINFORCEMENT VIA FRICTION STIR PROCESSING

Recent surface composite developments have impacted the aerospace, energy, and construction sectors. Friction Stir Processing (FSP) can manufacture high-quality surface composites from lightweight materials. This research optimizes process parameters, including Rotational Speed (RS), Travel Speed (TS), and Number of Passes (NoP), utilizing the design of experiments (DoE) statistical quality tool. The design matrix was created using the Response Surface Methodology (RSM) technique, and the experiments were based on the central composite design (CCD). ANOVA was used to validate the actual and projected models. Optimal FSP process parameters were utilized to create a surface composite of AA7075 with rGO and (rGO + MWCNT) reinforcements. The homogeneous reinforcement distribution on the surface composite was tested using optical microscopy. The average grain size of AA7075-T6 measured as 157±23 µm reduced to an average grain size of 7.5±1.2 µm for the rGO reinforced surface metal matrix composite (SMMC) and ultimately reduced to an average grain size of 6.5±0.7 µm for the (rGO + MWCNT) reinforced SMMC. The reduced fraction of intermetallic was identified in the microstructures, and the altered intensity of the significant XRD peaks was confirmed by X-ray Diffraction (XRD) analysis. Increased microhardness from 168±1.7 Hv (for BM AA7075-T6) to 190±2.4 Hv (for rGO reinforced SMMC) and further improved to a greater hardness of 196±1.8 Hv (for (rGO + MWCNT) reinforced SMMC). The impact strength improved drastically from 16±0.8 J (for BM AA7075-T6) to 21.3±1.1 J (for rGO reinforced SMMC) and greatly enhanced to 24±0.6 J (for (rGO + MWCNT) reinforced SMMC) were observed. The average thermal conductivity value of (rGO + MWCNT) reinforced SMMC showed a greater increase of 30-80 W/mK when compared to the BM. FSPed (rGO + MWCNT) SMMC specimen showed enhanced tribological properties with a reduction of nearly 65% compared to the BM. These results confirmed that the modified surface microstructures in the SMMCs by using FSP help to improve the characteristics of the AA7075-T6 alloy.

Keywords: Metal Matrix Surface Composites; Friction stir processing; Hybrid Reinforcement; Mechanical and Tribological properties; Thermal conductivity

1. Introduction

AA7075 alloy is preferred over other aluminum alloys in many applications due to its unique combination of properties like high strength-to-weight ratio, excellent fatigue resistance, good machinability and moderate density. Along with these properties, the AA7075 stands out among the others in terms of versatility in applications including aerospace, automotive, marine and defense sectors. Though it is a bit expensive than some other lower-strength aluminum alloys, it provides a cost-effective solution for applications where its superior performance justifies the higher material cost. AA7075 alone can have limited applications, but when it is combined with reinforcement particles, they can be adapted to various applications like landing gear parts in aircrafts, frame parts for the automotive chassis, armored vehicles and robotic arms because of its improved wear resistance and mechanical properties [1]. Composite materials may be developed using various methods [2-5]. Still, one of the most well-known methods for creating surface composites is Friction Stir Processing (FSP), which is built on its fundamental principles of Friction Stir Welding (FSW) [6-10]. Using the FSP approach, several researchers created surface composites. In their investigation of FSP on the AA7075 alloy, Suganeswaran et al. created a surface composite of SiC and $A1_2O_3$ reinforcement particles [11]. It was noted that the created hybrid surface composite had improved wear and microhardness characteristics. According to Jain *et al.* investigation into FSP on A5083-B_4C/SiC/TiC, the material's tensile, wear, and microhardness characteristics were all improved by the FSP [12]. After analyzing FSP on AISI420 martensitic stainless steel, Pan et al. concluded

[1] VIT-AP UNIVERSITY, SCHOOL OF MECHANICAL ENGINEERING, AMARAVATI, ANDHRA PRADESH, INDIA – 522237

* Corresponding author: sharma.ambuj@vitap.ac.in

that the treated material had increased hardness when compared to the material that had been traditionally hardened [13]. Similarly, Amra et al. found that the composite had better wear resistance qualities than the base material when they studied FSP on A15083/CeO_2-SiC [14]. Chen et al. revealed that the SiC-GNPs reinforced at 1.5 wt.% into the Al2024 metal matrix significantly enhanced the thermal conductivity of the material to an extent of 115% when compared to the Al2024 material [15]. Awad et al. key findings revealed that the graphite reinforced AA7075 composite produced by using two pass FSP has better wear resistance when compared to the BM AA7075 [16]. Using reinforcing materials to produce surface composite was the subject of several published investigations. Most of the researchers in the literature focused on examining the effects of variations in the hybrid reinforcement ratio across the FSP [17-23].

The DoE is an optimization approach that improves the statistical analysis method by supporting investigators in carrying out their experiments effectively using process variables. The welding process often challenges maintaining control of the process input parameters required to produce the desired mechanical properties like tensile strength and microhardness of the SMMCs. Different optimization techniques can be employed to define the desired output variables using mathematical models to characterize the link between input and output variables. The statistical optimization techniques were used to find the best FSP process parameters which helps to produce the best quality SMMCs. The RSM is used to investigate and optimize the impact of FSP process parameters on the build quality of the SMMCs [24]. The two response surface designs utilised in RSM are the CCD and the Box-Behnken design (BBD). The CCD method exhibits a more significant number of design points located beyond the boundaries of the cube, referred to as axial points. Additionally, CCD possesses significantly higher and lower settings compared to BBD. This characteristic enables CCD to effectively explore a wider range of regions to identify superior optimal solutions, utilizing the star points [25].

This study aims for the multi-objective parametric optimization of the FSP process and its characterization of the metallurgical, mechanical, thermal and tribological performance of surface composite AA7075-T6 with rGO and (rGO + MWCNT) reinforcements. As in the open literature, limited research was reported for these reinforcements. Therefore, the authors were motivated to conduct the current study to address the existing knowledge gap. Hence, the FSP was used to reinforce rGO and (rGO + MWCNT) into the surface of AA7075-T6 alloy to achieve grain refinement. After that, the role of modified microstructure on mechanical characterizations was examined.

2. Experimental procedure for Optimization of Process Parameters

The present investigation uses the RSM technique to explore the influence of FSP process parameters. The experiments were performed using an HMT milling machine equipped with a semi-automated linear movement configuration of the x-y-z axis. The process parameters that mainly influence the FSP technique are RS (Input X_1), TS (Input X_2), and NoP (Input X_3), which are considered for optimization in the present study. The process was carried out using a H13 steel tool having a shoulder Ø25 mm, a shank Ø18 mm, and a pin made in conical shape having a Ø7 mm at the top end and Ø3 mm at the bottom with a thread having a pitch of 0.5 mm and a total length of 4.7 mm respectively.

The base alloy AA7075-T6 sheet of 150×135×6.35 mm^3 was considered in this study. The elemental composition and mechanical properties of the base alloy material AA7075-T6 are represented in TABLES 1 and 2, respectively. The sheet was clamped to the bed of the milling machine with various clamps so there wouldn't be any movement of the plate while the process was being performed on the machine. The tool travelling was made in the X-direction till the end of the sheet, such that a greater number of samples were extracted to evaluate the mechanical properties of FSPed alloy material.

TABLE 1

Chemical composition of AA7075-T6 used in the investigation

Base Alloy	Zn	Mg	Si	Fe	Cu	Cr	Mn	Ti	Al
AA 7075-T6	4.8	2.5	0.25	0.11	1.40	0.18	0.05	0.07	Balance

TABLE 2

Mechanical properties of different grades of Al alloys used in the investigation

Material	Hardness (Hv)	Yield Strength (MPa)	Tensile Strength (MPa)	Elongation (%)
AA7075-T6	168	503	572	11

Determining the optimal process parameters plays a crucial role in the FSP technique, as it is essential for achieving higher mechanical properties. Only the most influential process parameters like RS, TS, and NoP were evaluated for this study. Process parameters that have a less significant role in controlling the FSP process, such as tilt angle of 3°, axial load of 5 kN, tool pin profile as a tapered cylindrical threaded tool, and insertion depth of 4.8 mm, were considered constant throughout the process.

2.1. Design of Experiments (DoE)

The DoE process involves strategically controlling various characteristics and influencing factors to observe corresponding changes in the output response. DoE strategy was used to estimate the optimal range of process parameters. The DoE method is a powerful tool for screening, modelling, and optimizing variables (i.e., outputs) by systematically changing process parameters. The systematic use of DoE is prevalent

in establishing a mathematical correlation between the FSP process parameters and the mechanical characteristics (output variables) of the FSPed components. This correlation is essential for selecting the best process parameters that produce the desired quality composites. The RSM is used to analyze the impact of independent process parameters and their corresponding effects on the response variables. The RSM analyses the impact of independent process variables and their corresponding effects on the response. The contour plot and the resulting three-dimensional surface plots depict the connection between the response and the input factors. The current study utilized a CCD to generate a quadratic model, a popular method for response surface designs [26-28]. The CCD can be rotated by adjusting the distance between two points equals to the $4\sqrt{F}$, where F represents the factorial points. The experiments were conducted to develop models from a three-factor, three-level, face-centred CCD factorial design.

2.1.1. Selection of input process parameters and responses

The FSPed composite's quality significantly depends on the input process parameters. The process parameter ranges were selected within a closer range based on the proceeding trial runs conducted before the experimentation. The preliminary experimental runs varied only one input parameter while maintaining the other process parameters constant. This determined the range within which the parameters could function effectively. The ranges of the selected parameters were determined through multiple trial runs and subsequent visual inspection of the onion rings and blow holes, if any, formed on the processed region. The working range was determined based on the visual examination of the processed layer surface for uniformity and its absence of visible defects. TABLE 3 specifies the established upper and lower limits for the FSP input parameters. The parameters of the independently controlled process, such as RS, TS, and NoP, were identified [29-31]. The chosen parameters for the experiment were an RS ranging from 900 to 1300 rpm, a travel speed of 40 to 60 mm/min, and no. of passes within the range of 1 to 3. In this RSM-based face-centred CCD design, the optimization was carried out using the three levels and 3-factor method.

TABLE 3

Input process parameters coded values and actual values for three levels and their ranges

Parameters	Symbols	Units	Levels		
			–1	0	1
Rotational Speed (RS)	X_1	rpm	900	1100	1300
Travel Speed (TS)	X_2	mm/min	40	50	60
No. of Passes (NoP)	X_3	number (no units)	1	2	3

TABLE 4 displays the coded and uncoded design matrix for the chosen process parameters and their units and notations. The design consists of 20 experimental runs. It presents the run order and the correspondence between coded and real values for the three factors in the Design-Expert software v.13 generated DoE, with an α value of 1. The study includes three levels of input process parameters and two desired output responses.

TABLE 4

Design of Experiment (DoE) runs to show the actual and coded values

Ex. No.	Rotational Speed (X_1) rpm		Travel Speed (X_2) mm/min		No. of Passes (X_3)	
	Value	Code	Value	Code	Value	Code
1	900	–1	60	1	3	1
2	1100	0	50	0	3	1
3	1100	0	50	0	2	0
4	1300	1	40	–1	1	–1
5	1100	0	50	0	2	0
6	1300	1	50	0	2	0
7	1100	0	50	0	2	0
8	900	–1	50	0	2	0
9	1300	1	60	1	3	1
10	1100	0	60	1	2	0
11	1100	0	50	0	2	0
12	1100	0	50	0	2	0
13	900	–1	40	–1	3	1
14	1300	1	40	–1	3	1
15	1100	0	50	0	1	–1
16	900	–1	40	–1	1	–1
17	1100	0	50	0	2	0
18	900	–1	60	1	1	–1
19	1100	0	40	–1	2	0
20	1300	1	60	1	1	–1

2.1.2. Measurement of Responses

20 experimental runs were performed using a design matrix, with randomization employed to reduce the possibility of introducing systematic errors into the system. The wire-cut electrical discharge machine (EDM) was used to extract the samples from the FSPed composites to evaluate their mechanical performance. Three samples were extracted to assess the tensile strength of the FSPed composites, and one sample was extracted to evaluate the FSPed composites' hardness from each experimental run specimen. Thus, the average of the results was considered for the final observations.

2.1.3. Development of mathematical model

The present responses were expressed as mathematical functions, where the process parameters were considered, the constituent factors denoted in the Eq. (1). The regression technique is used to construct the mathematical model to optimize the

tensile strength and microhardness. The response function that represents the FSPed composite optimization can be written as:

$$\text{Responses } y = f(X_1, X_2, X_3) \tag{1}$$

Where X_1, X_2 and X_3 are the RS in rpm, TS in mm/min and NoP respectively. The process is represented by a second-order polynomial equation assuming that a quadratic regression model can predict the response variable. The second-order mathematical equations from the RSM are presented in the Eq. (2).

$$y = \beta_0 + \sum_{i=1}^{q} \beta_i x_i + \sum_{i=1}^{q} \beta_{ii} x_i^2 + \sum_{i=1,\,(i<j)}^{q} \beta_{ij} x_i x_j + \epsilon \tag{2}$$

The variable q denotes the number of process variables, while β_0 and β_i represent the coefficients concerning the linear, quadratic, and interaction factors.

The mechanical characteristics of the FSPed composites, namely the tensile strength and microhardness were measured. The recorded output responses were displayed in TABLE 5 with the coded design matrix.

TABLE 5

Design a matrix with the measured output responses

Ex. No. (runs)	Process variables (coded)			Output measured responses	
	RS (X_1)	TS (X_2)	NoP (X_3)	Tensile Strength (MPa) (Y_1)	Microhardness (Hv) (Y_2)
1	–1	1	1	561	185
2	0	0	1	555	182
3	0	0	0	551	179
4	1	–1	–1	510	175
5	0	0	0	550	179
6	1	0	0	543	178
7	0	0	0	551	179
8	–1	0	0	556	181
9	1	1	1	557	182
10	0	1	0	558	181
11	0	0	0	550	179
12	0	0	0	550	179
13	–1	–1	1	556	183
14	1	–1	1	549	179
15	0	0	–1	532	177
16	–1	–1	–1	534	178
17	0	0	0	551	179
18	–1	1	–1	553	179
19	0	–1	0	544	178
20	1	1	–1	534	178

2.1.4. Parameters Optimization

A comprehensive quadratic model is subjected to an ANOVA analysis to evaluate the statistical significance of responses, with a confidence level of 95%. The *p*-value and correlation coefficient influence the model's accuracy and precision. The statistical significance of the relationship can be determined by evaluating the *p*-value. The generated model and its constants are compared to the standard 0.05 *p*-value, and significance is determined if the computed *p*-value is less than the standard value. The RS, TS and NoP play a crucial role in determining the tensile strength and microhardness of the FSPed composite. The multi-response objective function must consist of tensile strength and microhardness to achieve the best mechanical performance.

The specimens for the set of 20 experiments conducted using the above-selected process parameters are represented in Fig. 1 below.

2.2. Mathematical modelling of regression analysis

Numerical computation and analysis calculated the mathematical functions that govern the FSPed composite response variables. The regression model coefficients quantify the functional relationships between the FSP process parameters and mechanical characteristics. Regression analysis involves the development of an empirical mathematical model that establishes a correlation between the independent variables and the dependent response functions. The present study executed 20 experiments utilizing the RSM design matrix to establish the correlation between processing variables and output-measured responses. It is essential to highlight those alternative statistical approaches, such as Taguchi and full factorial, require 27 experiments. This emphasizes the benefits of utilizing the RSM design, which can decrease experimental time and expenses by saving around 37% of experimental runs. The quadratic model was optimal for predicting the suitable input parameter combinations based on the testing data results. The established equations help predict and optimize response variable output values. The regression models can be visually represented through a graphical depiction in the form of a 3D surface plot, which is plotted against the response variable and process parameters. These plots illustrate the correlation between the input variables and results. The second-order mathematical equation coefficients were determined using the least squares method. The equation for the second-order quadratic response surface model with all coefficients of the developed model is given below in the Eq. (3) [32-34]. It explains the relationship between the process variables and the response functions.

$$y = \alpha_0 + \alpha_1 x_1 + \alpha_2 x_2 + \alpha_3 x_3 + \alpha_{11} x_1^2 + \alpha_{22} x_2^2 + \\ + \alpha_{33} x_3^2 + \alpha_{12} x_1 x_2 + \alpha_{13} x_1 x_3 + \alpha_{23} x_2 x_3 \tag{3}$$

where

α_0 – free term of the regression equation,
$\alpha_1, \alpha_2, \alpha_3$ – linear terms,
$\alpha_{11}, \alpha_{22}, \alpha_{33}$ – quadratic terms,
$\alpha_{12}, \alpha_{13}, \alpha_{23}$ – interaction terms.

The present study examines the relationship between the response variables, namely tensile strength (Y_1), and microhardness (Y_2) with the independent variables of RS (X_1), TS

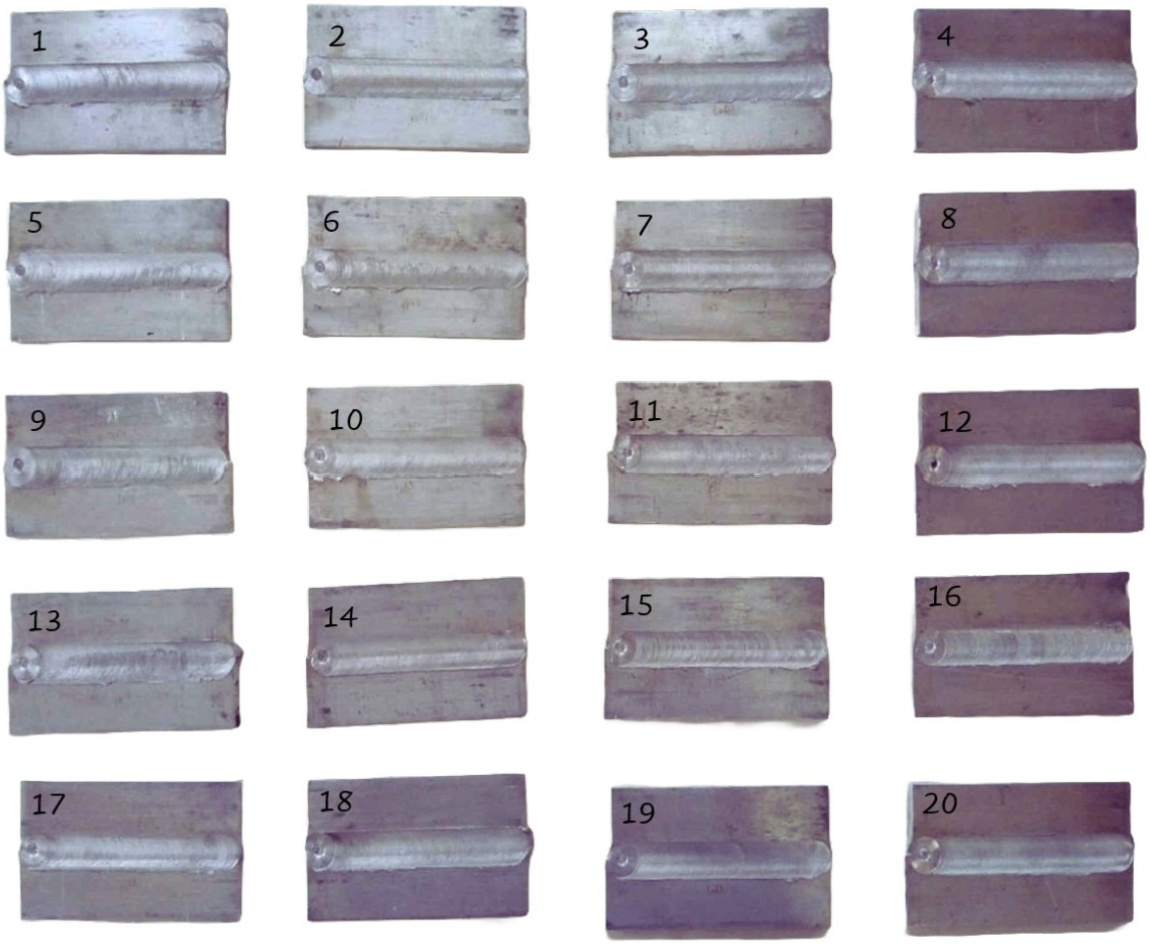

Fig. 1. A set of experiments was conducted using the selected process parameters

(X_2), and NoP (X_3). The mathematical models were developed after the coefficients were determined. To establish correlations between process parameters and responses as expressed in the mathematical model for output responses. The developed mathematical model for tensile strength and microhardness has been formulated and presented in Eqs. (4), and (5). The coefficient values corresponding to the various responses have also been established. The resulting mathematical model has been provided for predicting tensile strength and microhardness measurements.

$$\begin{aligned}\text{Tensile strength} = 550.32 - 6.70x_1 + 7.00x_2 + 11.50x_3 + \\ + 1.0000x_1x_2 + 4.00x_1x_3 - 3.75x_2x_3 - 0.5455x_1^2 + \\ + 0.9545x_2^2 - 6.55x_3^2\end{aligned} \quad (4)$$

$$\begin{aligned}\text{Microhardness} = 179.09 - 1.40x_1 + 1.20x_2 + 2.40x_3 + \\ + 0.3750x_1x_2 - 0.3750x_1x_3 + 0.1250x_2x_3 + \\ + 0.2727x_1^2 + 0.2727x_2^2 + 0.2727x_3^2\end{aligned} \quad (5)$$

2.3. Statistical Analysis of ANOVA approach

ANOVA is used to identify the process parameter's main effects and interactions that are essential to the response characteristics. The input variables statistically significant on the output measure have been determined using the ANOVA approach. An empirical relationship between inputs and output variables was established, and its functions were evaluated. The statistical significance of model terms is determined by the *p*-value, which is expected to be less than 0.05. The presented model was sufficient at a 95% confidence level. According to TABLES 6 and 7 of the ANOVA analysis of tensile strength (Y_1), and microhardness (Y_2), the *p*-value for the model has been determined as 0.0001. This result indicates that the model generated is statistically significant in establishing a correlation between the input variables and output responses. The obtained model and process parameters are considered significant because the *p*-value in ANOVA is less than 0.05. A non-significant lack of fit is acceptable for optimum model development. The obtained *F* values of 1082.81 and 187.82 for the tensile strength and microhardness, respectively, indicate the statistical significance of the models. As the *F* value is attributed to noise, the probability of its occurrence is only 0.01%. In this model, the calculated R^2 values of Y_1, and Y_2 were 0.9990, and 0.9941. The degree of precision connected to the predicted R^2 values of Y_1 and Y_2 are 91.64% and 82.40% when compared with the adjusted R^2 values of Y_1 and Y_2 are 96.75% and 95.23%, which is considered acceptable to the support developed mathematical model. The R^2 coefficient provides a representation of the effective level of fitness functions. The adjusted R^2 values of Y_1

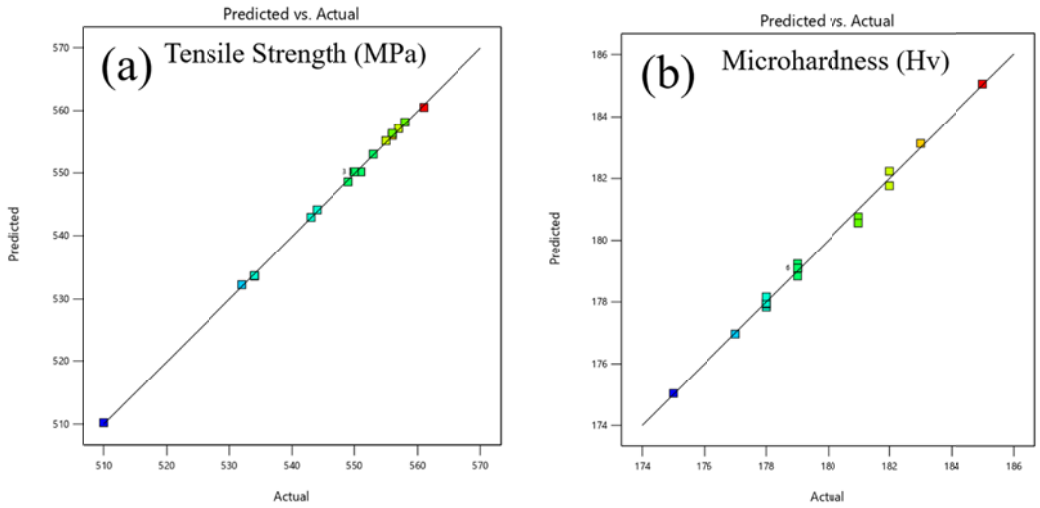

Fig. 2. Normal effect plots for Predicted vs Actual value graphs for (a) Tensile Strength and (b) Microhardness

TABLE 6

Tensile Strength ANOVA analysis

Source	Sum of Squares	df	Mean Square	*F*-value	*p*-value	Significant
Model	**2710.97**	**9**	**301.22**	**1082.81**	**<0.0001**	
X_1 – Rotational Speed	448.90	1	448.90	1613.69	<0.0001	
X_2 – Travel Speed	490.00	1	490.00	1761.44	<0.0001	
X_3 – No. of passes	1322.50	1	1322.50	4754.08	<0.0001	
X_1X_2	8.00	1	8.00	28.76	0.0003	
X_1X_3	128.00	1	128.00	460.13	<0.0001	
X_2X_3	112.50	1	112.50	404.41	<0.0001	
X_1^2	0.8182	1	0.8182	2.94	0.1171	
X_2^2	2.51	1	2.51	9.01	0.0133	
X_3^2	117.82	1	117.82	423.53	<0.0001	
Residual	2.78	10	0.2782			
Lack of Fit	1.28	5	0.2564	0.8545	0.5664	not significant
Pure Error	1.50	5	0.3000			
Cor Total	2713.75	19				
Std. dev	0.5274	**R^2 = 0.9990**	**Adjusted R^2 = 0.9981**	**Predicted R^2 = 0.9936**		

and Y_2 are 0.9981 and 0.9888, exhibiting a degree of closeness to the predicted R^2 values of Y_1 and Y_2 as 0.9936 and 0.9405, respectively. The data collected from experiments agree with the data predicted by the developed model. The empirical models established exhibit a near-perfect correlation, as shown by the distribution of observed and predicted values of the responses along the 45-degree line. The two-dimensional graphical normal effect plot shown in Fig. 2(a,b) demonstrates higher accuracy between the actual and predicted values. The response surface model has significantly correlated the input and output factors.

A statistical analysis using the ANOVA test was conducted to verify the accuracy of these empirical equations. The ANOVA statistical method is employed to identify the significant variables that influence the output responses, as well as to assess the adequacy of the model that has been developed. The significance of mathematical models, model coefficients, and lack-of-fit tests have been explored. TABLES 6 and 7 present the response surface design CCD model results of the ANOVA for the responses and indicate the statistically significant models ($p < 0.05$) at a confidence level of 95%.

Further, Eq. (6) calculates the contribution percentage for each process parameter and its interaction.

$$Percentage\,of\ contribution = \\ = \frac{Sum\,of\ square\,value\ for\ each\ parameters}{Total\ sum\,of\ square} \tag{6}$$

The results of the ANOVA show that the NoP (X_3) significantly influences the FSPed specimen's tensile strength (Y_1) and hardness (Y_2), contributing to 48.73% and 59.38%, respectively.

The perturbation plot is a graphical representation that illustrates the impact of individual factors on the responses. The perturbation plots for the tensile strength and microhardness are shown in Fig. 3(a, b). The RSM model selects the default reference point in the centre of the design space. Therefore, it is evident from the graphs that the NoP significantly influences the tensile strength and microhardness of the FSPed specimens.

The confirmation test was conducted using the best of these optimal parameters, and the results were considered satisfactory. The regression Eqs. (4) and (5) are used as predic-

TABLE 7

Microhardness ANOVA analysis

Source	Sum of Squares	df	Mean Square	*F*-value	*p*-value	Significant
Model	**96.43**	**9**	**10.71**	**187.82**	**<0.0001**	
X_1 – Rotational Speed	19.60	1	19.60	343.59	<0.0001	
X_2 – Travel Speed	14.40	1	14.40	252.43	<0.0001	
X_3 – No. of passes	57.60	1	57.60	1009.72	<0.0001	
X_1X_2	1.13	1	1.13	19.72	0.0013	
X_1X_3	1.13	1	1.13	19.72	0.0013	
X_2X_3	0.1250	1	0.1250	2.19	0.1696	
X_1^2	0.2045	1	0.2045	3.59	0.0875	
X_2^2	0.2045	1	0.2045	3.59	0.0875	
X_3^2	0.2045	1	0.2045	3.59	0.0875	
Residual	0.5705	10	0.0570			
Lack of Fit	0.5705	5	0.1141			
Pure Error	0.0000	5	0.0000			
Cor Total	97.00	19				
Std. dev	0.2388	**R^2 = 0.9941**	**Adjusted R^2 = 0.9888**	**Predicted R^2 = 0.9405**		

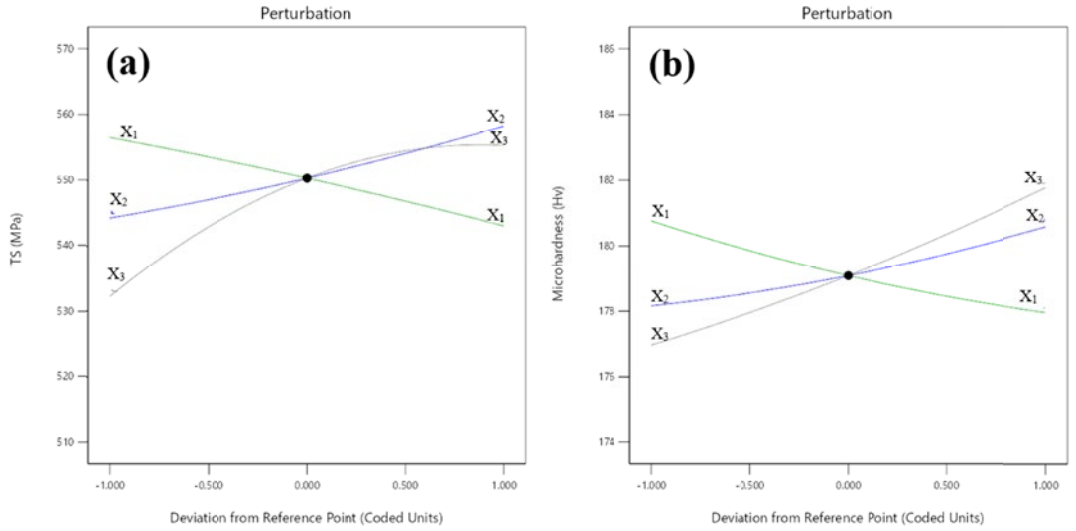

Fig. 3. Perturbation plots for (a) tensile strength and (b) microhardness

tive models for tensile strength and microhardness responses. The predicted models for the FSP technique accord quite well with the experimental results. The adequacy of the model was evaluated by conducting confirmatory tests. These experiments involved using newly selected independent variables within the experimental range. Thus, the confirmatory results are shown in the below TABLE 8.

The experimental results for validating the optimal FSP process parameters are compared with the predicted optimal parameters using the RSM method. The results and error percentages obtained between experimental and predicted models for optimized input parameters are presented in TABLE 8. The predictive models exhibit high acceptance of the experimental findings associated with FSP process parameters. This study uses these process parameters to fabricate AA7075-T6 SMMCs using different reinforcements and evaluate their mechanical and microstructural characteristics.

TABLE 8

Confirmatory test results

Optimized results	Input Process Parameters			Output characteristics	
	Rotational Speed	Travel Speed	No. of Passes	Tensile Strength	Microhardness
RSM – Predicted	1100	50	2	550.318	179.091
Experimentally measured				551	179
Error (%)				0.12	0.05

3. Fabrication of FSPed AA7075-T6 metal matrix surface composites

AA7075-T6 plate (150 mm × 75 mm × 6.35 mm) was used as a base specimen. Particles of rGO (Purity – 99%) with dimensions (X & Y) – 5-10 µm, thickness (Z) – 0.8-2 nm, number of layers – 1-3, and oxygen content of 5 % considered. Along with the rGO, particles of MWCNT (Purity – 99%) with a diameter of 10-20 nm and length – 10 µm were considered. These two particles were used to reinforce the surface of the AA7075-T6 alloy to prepare SMMCs. A 2 mm square groove was made on the centre surface of the base alloy plate. Reinforcement powders were compacted as per the volume proportions of rGO and MWCNT, which were extensively used to fabricate the SMMCs ($S_3 - S_4$), respectively, as shown in TABLE 9. This study also compared the base material and the base plate without reinforcement (S_1 and S_2) with the reinforced samples ($S_3 - S_4$). Processing techniques like FSP have practical limitations regarding the volume fraction of reinforcements. High concentrations of nanomaterials can lead to processing difficulties such as poor dispersion, increased viscosity, or defects in the composite. The selected percentages are likely chosen to ensure the materials can be processed effectively and uniformly. The chosen concentrations of 10% rGO for S_3 and 5% each of rGO and MWCNT for S_4 are likely to strike a balance between enhancing the mechanical and electrical properties of the AA7075 matrix while avoiding potential agglomeration or dispersion issues that could arise with higher concentrations. Once the groove was made and packed with the reinforcement particles into it, a pin-less tool was processed on the top surface of the plate at the centre to eliminate the splashing of the particles during the processing. Further, a tapered cylindrical threaded tool made of H13 steel tool, which was used for the optimization technique, was again considered for the fabrication of SMMCs using the FSP technique. From the above section 2 of optimization of process parameters, it was clear that the RS of 1100 rpm, TS of 50 mm/min and NoP as two passes were maintained constant throughout the fabrication. The other parameters like tool tilt angle of 3°, plunge depth of 0.1 mm, tool penetration depth of 4.7 mm and axial load of 5 kN were maintained constant throughout the fabrication of SMMCs using the FSP technique. Therefore, one pass with the pin-less tool was passed on the groove surface and two passes with the tapered cylindrical threaded tool was stirred into the packed surface to effectively reinforce the particles into the MMC.

TABLE 9

Details of the specimen numbers along with the reinforcement volume ratios

Specimen name	The volume percentage of reinforcement	
	rGO (vol%)	MWCNT (vol%)
S_1	AA7075-T6	—
S_2	FSPed AA7075-T6	—
S_3	10	0
S_4	5	5

The sample S_4 is considered as a mixture of both rGO and MWCNT, a shift-speed ball milling technique was utilized to make a uniform mixture. For this study, zirconia balls with different diameters like 3 mm and 6 mm were used at ratio of 1:3. Then the ball-powder ratioof 8:1 was considered to seal it in a agate jar filled with Ar. Then they were milled at 120 rpm for 6 hours, then increased to a speed of 250 rpm for another 2 hours. Once the ball milling was finished, the intermix powder was rested for a longer duration before using it as a reinforcement into the metal matrix. The schematic representation of the FSP process for fabricating the samples was presented in detail in Fig. 4. The test samples for the characterizations were extracted from the Stir Zone (SZ) of the fabricated samples. All the specimens are cut cross-sectionally from the region of SZ using wire-cut EDM, and respective samples are polished using different emery papers (180-2000 grit size) and etched for 10 seconds using the Kellers reagent (4 ml hydrofluoric acid, 6 ml hydrochloric acid, 8 ml nitric acid, and 82 ml distilled water) before testing. The morphological examinations are carried out using an optical

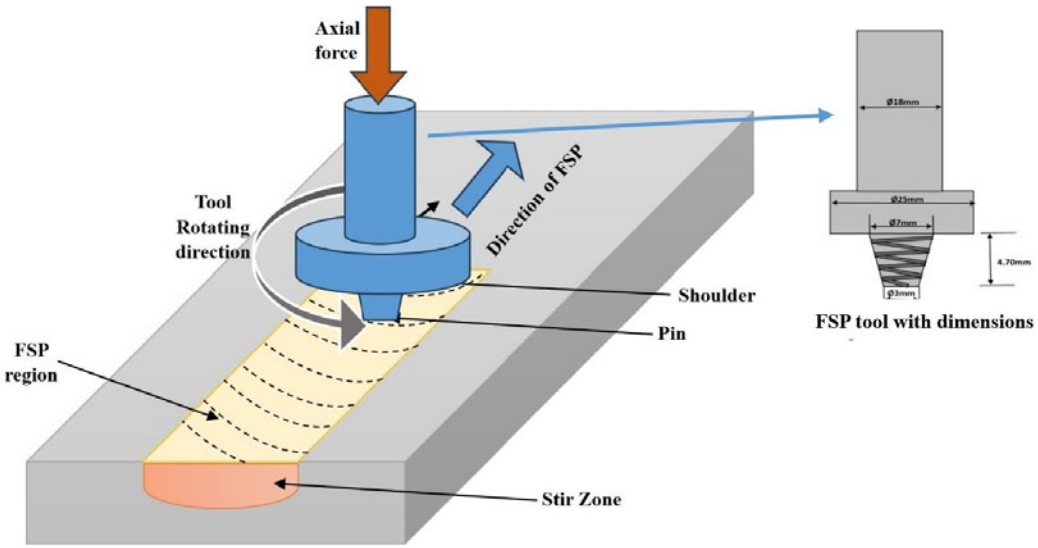

Fig. 4. Schematic representation of the FSP process

microscope (OM) (MAKE: COSLAB CIM100 Inverted Metallurgical Microscope) and SEM equipment (MAKE: ZEISS EVO 10) to evaluate the build quality of the fabricated specimens. Along with the morphological evidence, the grain size evaluation was also carried out to verify the correlation with the mechanical properties. The XRD (MAKE: RIGAKU MiniFlex) is also used to analyse the elements and the respective phases present in fabricated specimens. The mechanical characteristics are evaluated using tensile strength (MAKE: Tinius Olsen H10KL), microhardness (MAKE: Micro Vickers Hardness tester) and impact strength (MAKE: Digital Impact Testing Machine).

The thermal conductivity of the fabricated samples has been measured in the present experimental investigation using a specially designed thermal conductivity experimental apparatus. A specimen measuring 15×15×5 mm was sectioned for thermal conductivity examination. The top and bottom surfaces of the work specimens were measured for temperature using a K-type thermocouple (accuracy±1°C). Measurements were made between the temperatures of 30 to 400°C using a steady voltage source, for 15 minutes. Observations were repeated for almost all levels of voltages starting from 50 V to 230 V with maintaining an equal interval of about 50 V. At the lowest voltage of 25 V, it has little or no impact on thermal conductivity. Different degrees of heat input were used to measure the various surface temperatures. The specimens' thermal conductivity was assessed using the Cartesian coordinate equation (Eq. (7)).

$$Q = kA\frac{dT}{dx} \tag{7}$$

where Q is represented by the heat transfer rate ($V \times I$) in W, k by the thermal conductivity in W/mK, A by the work specimen's cross-sectional area in m^2, dT by the temperature differential between the specimen's top and bottom surfaces in K, and dx by the specimen's thickness in m. A Thermomechanical Analyzer (TMA Q400) setup with a 10°C/min heating rate, 0.1 N applied force, and a 300-670 K temperature range is used to test the specimens' CTE.

The specimens (5×5×5 mm) were sectioned across the SZ, and a pin-on-disc tribometer (MAKE: DUCOM TR-20-LE) was used to measure the wear rate. A counter disc portion manufactured of EN31 steel with a hardness of 60 HRC is taken into consideration, and the ratio of volumetric loss to sliding distance is used to calculate the specimen wear rate. Next, the average of three wear results is considered, and these data are recorded for a sliding distance of 2000 m, a load of 60 N, and a sliding velocity of 650 rpm. The scratch test was performed on all the FSPed specimens along with the BM AA7075-T6. To examine the variation in scratch hardness between the FSPed specimens and the BM AA7075-T6, the stroke length was set as 10 mm within the SZ for each specimen. To assess the specimens' coefficient of friction (CoF) and traction force (TF), the scratch was performed with a sliding velocity of 1 mm/s at a constant load of 30 N was applied. An optical microscope was used to examine the profiles of the scratch tracks. Five different locations on the specimens were averaged to determine the width of each scratch.

4. Characterization of fabricated surface metal matrix composites

4.1. Microstructural observations

Microstructural images shown in the below Fig 5. are generated using Coslab CIM-100 inverted metallurgical microscope at 100 µm at 200× magnification. All the FSPed samples showed clear microstructure modification compared to base metal because of the dynamic recrystallization during FSP [35]. The grain size was calculated using the line interceptor method in Coslab Image Analysis software by a conversion scale of 2 pixels per micron. Microstructures usually hold great importance when analyzing the processing effect of the FSP. On evaluating the Figs. 5(a) and 5(b), it can be concluded that there is an extreme plastic deformation and grain refinement in base material AA7075-T6 when processed using FSP. Further, in Fig. 5(c), the grain refinement has improved after the reinforcement of rGO particles into the base matrix. The grain size has reduced more after the FSP with the reinforcement. Furthermore, in Fig. 5(d), the grain refinement has improved significantly after the hybrid reinforcement of (rGO + MWCNT) nanoparticles into the base matrix. Various mechanisms and factors affect grain refinement during the FSP, such as (i) dynamic recrystallization and dynamic recovery (related to process parameters) and (ii) the Zener pinning effect and particle-stimulated nucleation (related dispersion of particles). The material experiences severe plastic deformation, leading to dynamic recrystallization in the NZ, resulting in higher grain refinement. Aluminum alloys are associated with high stacking fault energy, leading to dynamic recovery and rearranging dislocation. This successive dislocation accumulation generates the fine equiaxed grain in NZ. The intense stirring action of the tool breaks up the reinforcement particles into small fragments, inhibiting grain growth. This grain size reduction is responsible for the Zener pinning effect [36]. The grain size of the BM AA7075-T6 was observed an average of 157±23 µm. The average grain size for a single-pass FSP was 12.5±2.1 µm, and the two-pass FSP measured 9.5±1.8 µm respectively, without introducing any reinforcements. The smaller grain size is achieved due to the sufficient stirring produced by the tool to settle the reinforcement particles in a homogenous nature during FSP [37]. However, the reinforced FSP specimens S_3 and S_4 with rGO and (rGO + MWCNT) reinforced samples were measured with an average grain size of 7.5±1.2 µm and 6.5±0.7 µm, respectively. As there is an extra pass for packing the reinforcement particles into the groove was made for samples S_3 and S_4, it helped for the uniform dispersion of the reinforced particles and dynamic recrystallization within the SZ using the multipass FSP. The added reinforcement particles act as a nucleating site for new grain and hindered grain boundary formation during FSP [38].

The morphological analysis was conducted utilizing SEM equipment (MAKE: ZEISS EVO 10), with results illustrated in Fig. 6(a-d). In Fig. 6(a), the base material BM AA7075-T6 exhibits a coarse grain structure characterized by numerous agglomerations and pores. Upon subjecting the BM to FSP, as

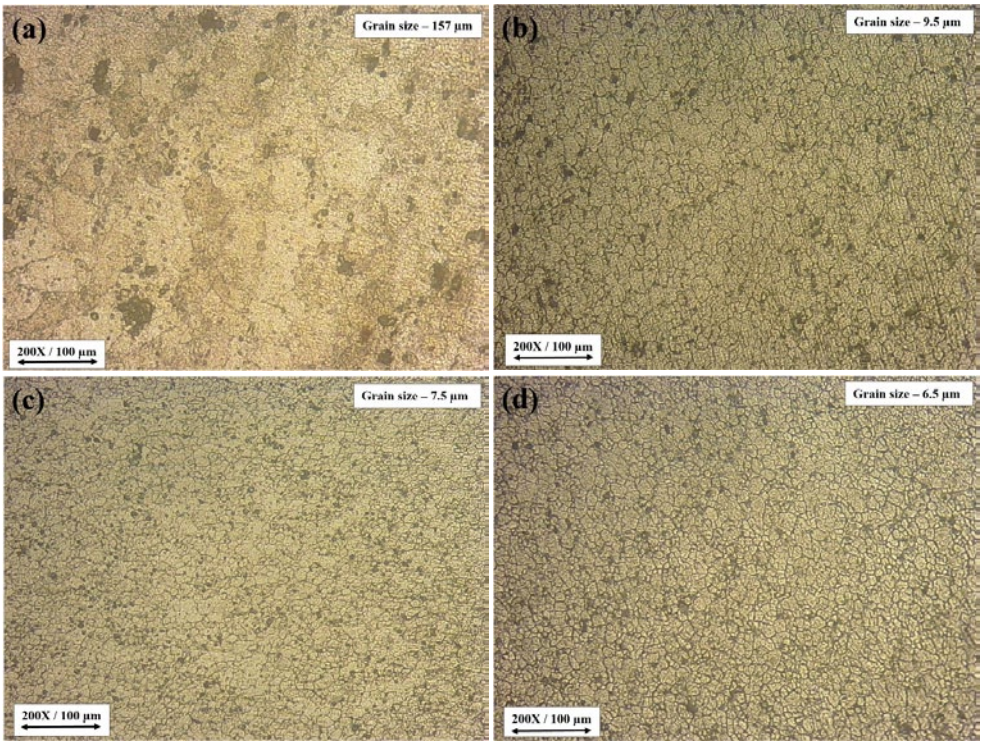

Fig. 5. Optical Microstructures of samples at 100 µm (a) S_1, (b) S_2, (c) S_3, (d) S_4

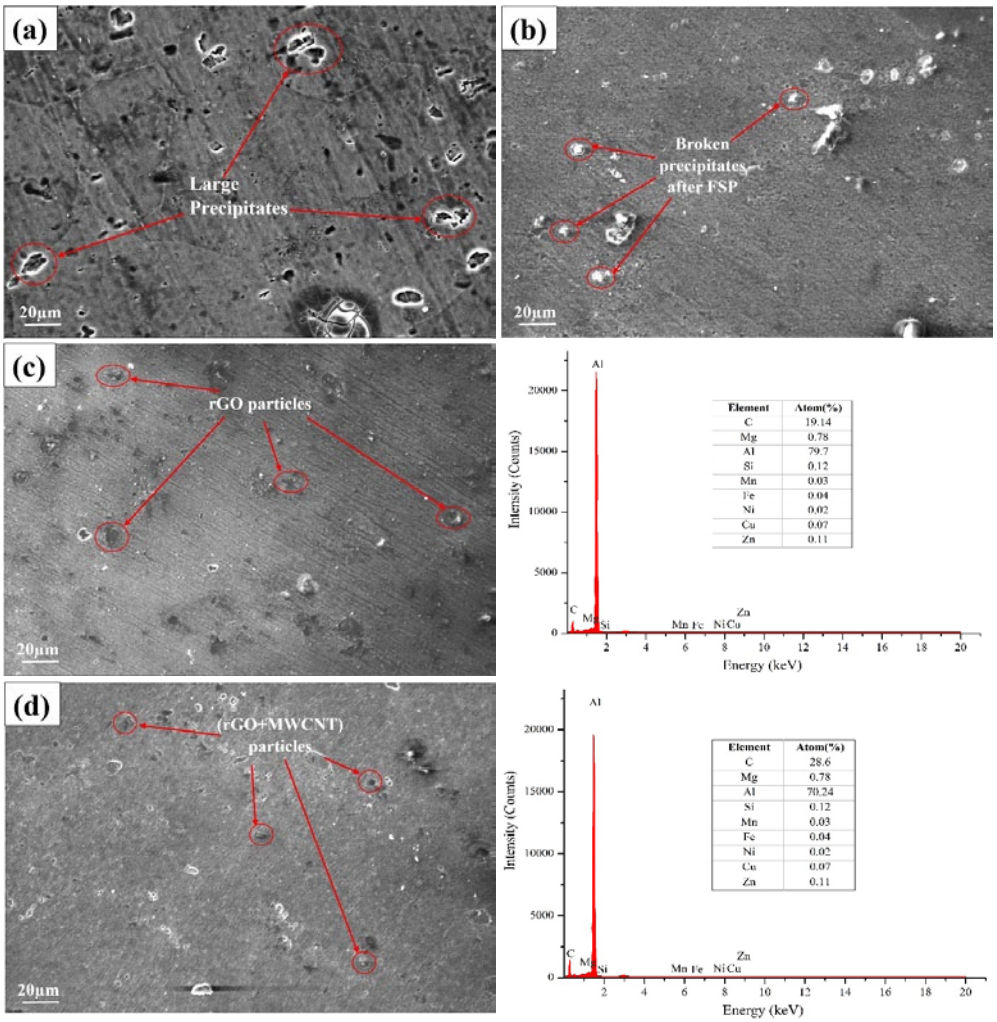

Fig. 6. SEM images of samples at 20 µm (a) S_1, (b) S_2, (c) S_3 with EDS, (d) S_4 with EDS

depicted in Fig. 6(b), as the coarse grains transform into finer, also large precipitates broken into finer precipitates within the FSPed zone. This transformation is attributed to the combined effects of frictional heat, plastic deformation, dynamic recrystallization, and particle-induced nucleation occurring during the FSP process. Furthermore, the reinforcement of rGO particles into the metal matrix, along with an increased number of FSP passes, results in enhanced dispersion of the reinforcement particles and a reduced quantity of precipitates, as evidenced in Fig. 6(c) with EDS. Subsequently, incorporating a hybrid reinforcement of both rGO and MWCNTs into the same matrix further reduces the presence of precipitates and promotes a more uniform distribution of nanoparticles observed in Fig. 6(d) with EDS. Additionally, multipass FSP contributes to a significant reduction in grain size within the FSPed zone. Overall, the SEM observations indicate a homogeneous dispersion of rGO reinforcements on the metal matrix surface, devoid of any noticeable defects. This uniform dispersion is anticipated to positively impact the mechanical properties of the material, thereby enhancing its overall performance.

4.2. XRD Analysis

The XRD technique is an important phase analysis method in the SMMCs to determine the reaction between the alloy and ceramic components. The XRD results of all the samples S_1 to S_4 are represented in Fig. 7. The XRD peaks for aluminum are observed in both S_1 and S_2 samples without any significant differences. The intermetallic peaks were observed for the reinforced FSP composites S_3 and S_4, respectively. As the rGO and MWCNT particles are the compounds of carbon elements, the carbon peaks were observed in both S_3 and S_4 samples. As the reinforced composites include carbon peaks, it was also observed that the actual aluminum peaks were shifted a bit when compared to the other two base specimens. This XRD pattern confirms the presence of AA7075, rGO and MWCNT particulates in the composite, which were indexed using the JCPDS data obtained.

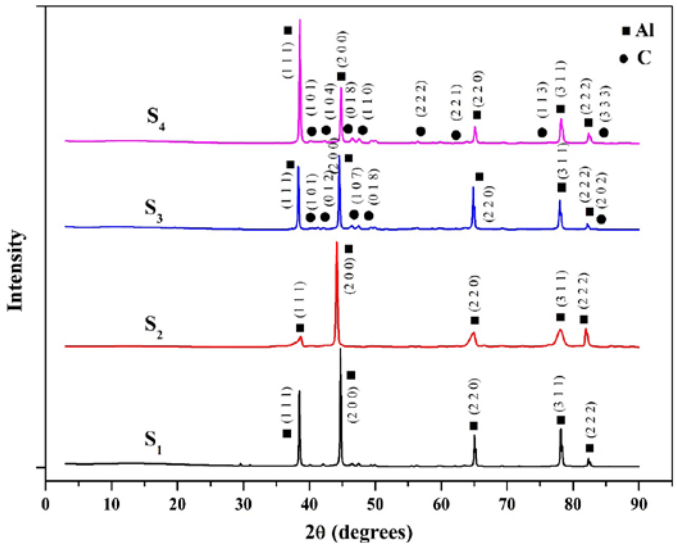

Fig. 7. XRD patterns of all the samples

4.3. Tensile Strength and Fractography

The effect of FSP and addition of reinforcements into the base material are illustrated in Fig. 8. From the figure, it was evident that the yield strength and UTS of the FSPed and reinforced samples (S_2, S_3, and S_4) were reduced to a little extent when compared to the base material AA7075-T6 (S_1). The reduction in the tensile strength depends on many microstructural features such as dislocation density, grain size and reinforcement interaction with the base metal matrix. The slight reduction of UTS may be attributed to the matrix softeneing caused due to FSP technique. The further reduction in UTS for the reinforced samples was observed with an increase in the elongation. Yuvaraj et al. [39] and Butola et al. [40] obtained similar results in their studies on aluminum composites. Due to the addition of rGO and MWCNTs into the base material causes dislocations within the crystal structure and further with the addition of FSP processing results in the reduction of grain size helps to enhance the ductility of the samples which can be further observed in the fractograhies.

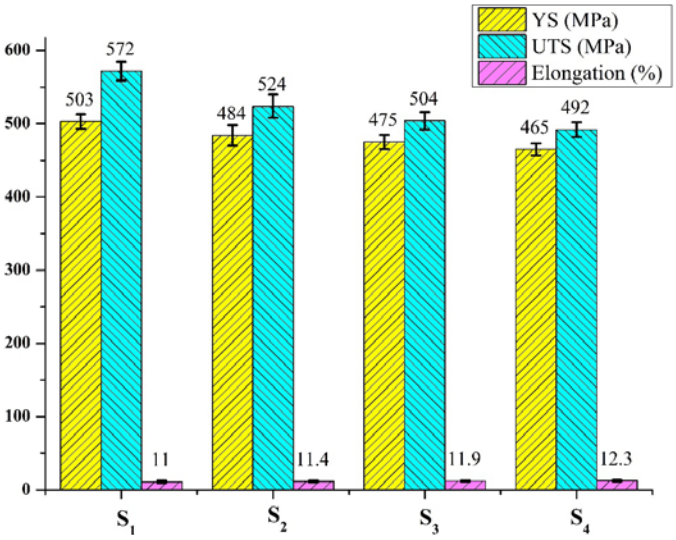

Fig. 8. Tensile test results of all the samples

Fig. 9(a-d) depicts the fractography of the raptured surfaces of the samples S_1 to S_4. The rapture occurred close to the centre of sample S_1 for base material, whereas for the other samples S_2 to S_4, the rapture occurred towards the direction of the HAZ as the microhardness was slowly reducing towards the outer region of the SZ. A shear plane with a cup cone shape was formed along the edges of the fractured samples. The ductile failure with honeycomb dimples was found in all the samples, where the size of the dimple decreased in order from S_1 to S_4, like the grain sizes found in the specimens. This indicates the distinct cleavage and plastic deformation characteristics due to the evenly distributed rGO and MWCNT reinforcing particles and a finer grain structure achieved through effective material mixing in the FSP.

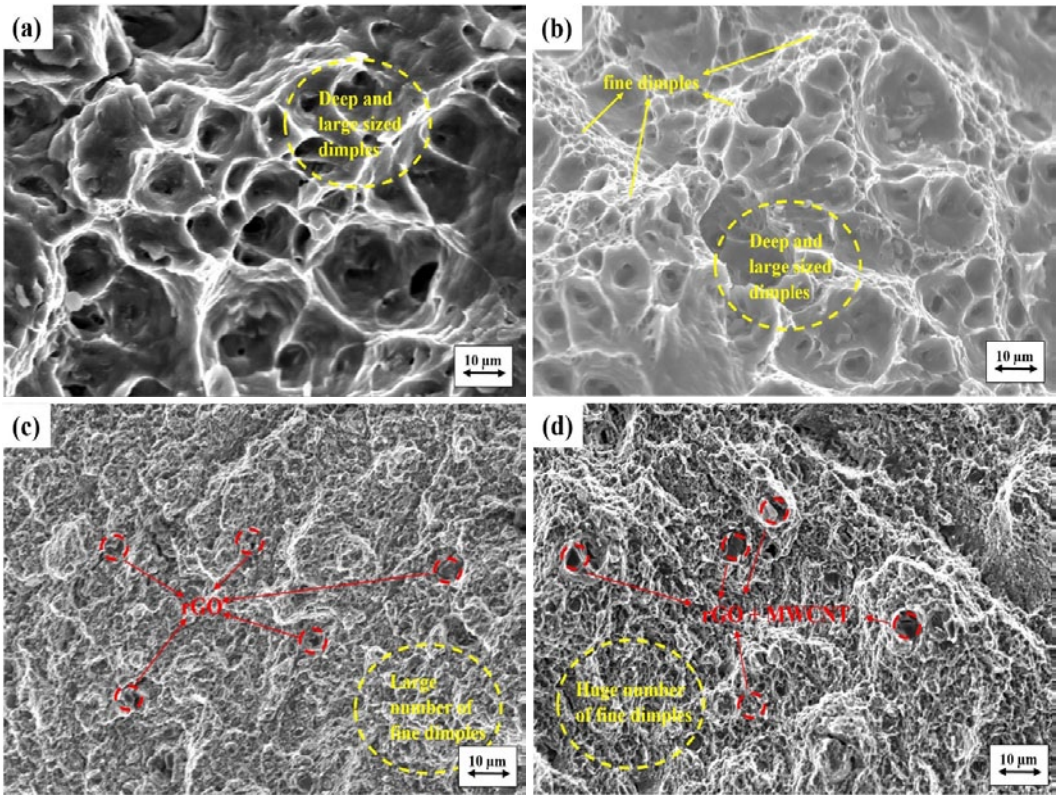

Fig. 9. SEM micrographs of the fractured surfaces of the tensile specimens: (a) S_1, (b) S_2, (c) S_3, (d) S_4

4.4. Microhardness Analysis

The bar chart shown in Fig. 10 of the microhardness of BM AA7075-T6, and other samples are reported, respectively. It can be observed that the minimum microhardness recorded was for BM AA7075-T6 (S_1), having a value of 168 Hv. Recorded microhardness for FSPed sample with two passes (S_2), having a value of 182 Hv; this enhancement in microhardness compared to sample S_1 because of the grain refinement due to processing. Also, it can be correlated with the grain size analysis presented in section 4.1. Microhardness of the sample S_3 reinforced with the 10 vol% rGO particles recorded an average hardness value of 190 Hv; this increased hardness value is attributed to well-dispersed rGO particles in the matrix. Microhardness of the sample S_4 reinforced with 5 vol% rGO particles and 5 vol% MWCNT particles into the Al matrix showed a microhardness value of 196 Hv. Compared to the microhardness value of all the samples, it can be concluded that the enhanced microhardness value in the hybrid MMCs might be because of the reinforcement particles in the Al matrix. The improvement in the hardness depends on (i) grain refinement due to dynamic recrystallization (as per the Hall-Petch relation) and (ii) uniform distribution of the reinforcement particles (as per Orowan strengthening) [41]. During FSP, higher heat in the tool shoulder and pin resulted in higher plastic deformation. Thus, dynamic recrystallization results in small grains. In FSP, grain refinement in the work material is responsible for improving hardness. The hall-patch relationship says that hardness is reliant inversely on the grain size [42]. According to the Hall-Petch relation, grain refinement during FSP improves the mechanical properties. Based on the Orowan strengthening mechanism, the uniform dispersion of the particle inside the NZ enhances the microhardness of the BM [43].

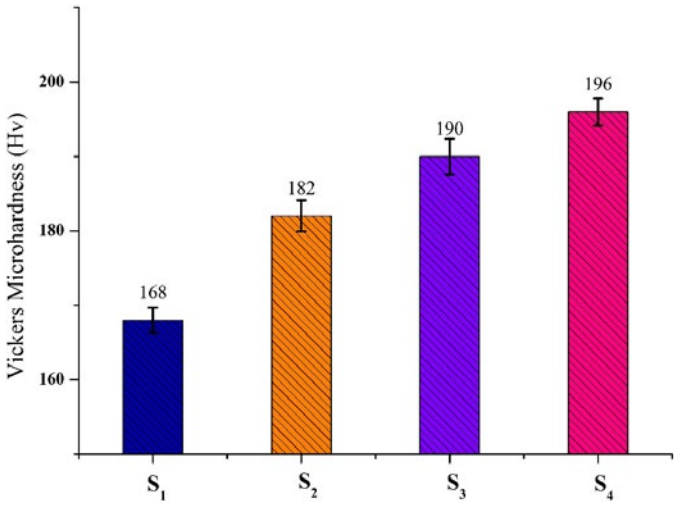

Fig. 10. Microhardness was reported for all samples

4.5. Impact Strength and Fractography

The Charpy test was conducted successfully for samples S_1 to S_4; their results are displayed in Fig. 11 respectively. The impact toughness energy for the BM was observed as 16 J, and the value of the FSPed sample without any reinforcement, i.e.,

S_2, was observed as 19.2 J. The FSPed specimens with the reinforcement rGO alone were observed as 21.3 J, and the hybrid reinforced (rGO + MWCNT) sample was observed as 24 J (50% increase compared to the BM). The reason for the improved impact toughness energy can be correlated with the grain size decrement and the elongation % increment with the addition of the reinforcements.

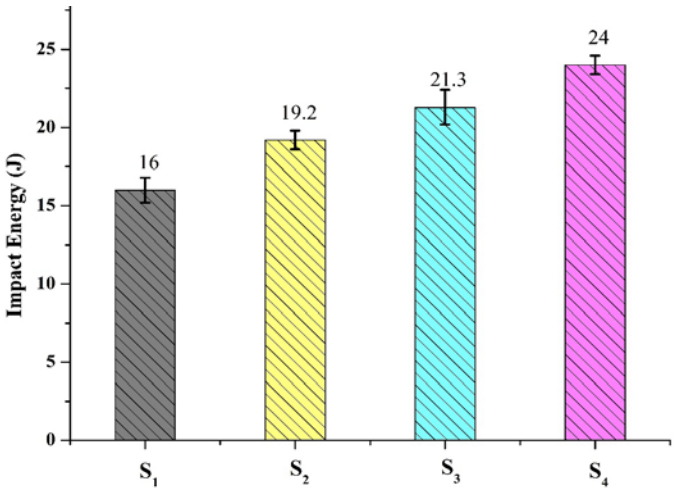

Fig. 11. Impact energies of all the samples

Fig. 12(a-d) shows the SEM fractographies of the fractured impact test samples of S_1 to S_4 respectively. In the case of the impact test, the fracture becomes shear-induced, and the strain rate remains high, unlike the tensile test specimens. In the case of the fractured impact test sample of BM, the fracture morphology differs at various locations of the specimen, shown in Fig. 12(a), due to non-uniform stress distribution throughout the specimen. Fine dimples rarely appear on this fractured surface, showing large-sized voids and inter-dendritic cracking. This kind of fracture was due to the coarse grains of the BM. This fracture morphology changed significantly for the FSPed samples S_2 to S_4 as shown in Fig. 12(b-d). The fracture surface of specimen S_2 exhibits finer dimples when compared to the sample S_1. At the same time, the reinforced FSPed samples S_3 and S_4 exhibit relatively higher toughness values and the fractured surfaces exhibit finer dimples in which the presence of plastic deformation before the fracture can be observed.

4.6. Thermal conductivity and CTE measurements

The heat transfer properties of BM AA7075-T6 and the FSPed specimens were determined from a temperature range of 30 to 400°C and plotted in Fig. 13(a-d). Initially, at a lower voltage of 25 V, the setup displayed a negligible temperature difference because of the small change in molecular momentum. As a result, we maintain a voltage level between 50 V and 200 V at 50 V intervals. As the voltage increases, the material heats up. The average thermal conductivity value for BM is 146.5 W/mK. The microstructural study of the FSPed specimen shows that there are more grain boundaries, which scatter photons and electrons more widely. This phenomenon leads to a decrease in the heat transportation behavior of the FSPed specimen in com-

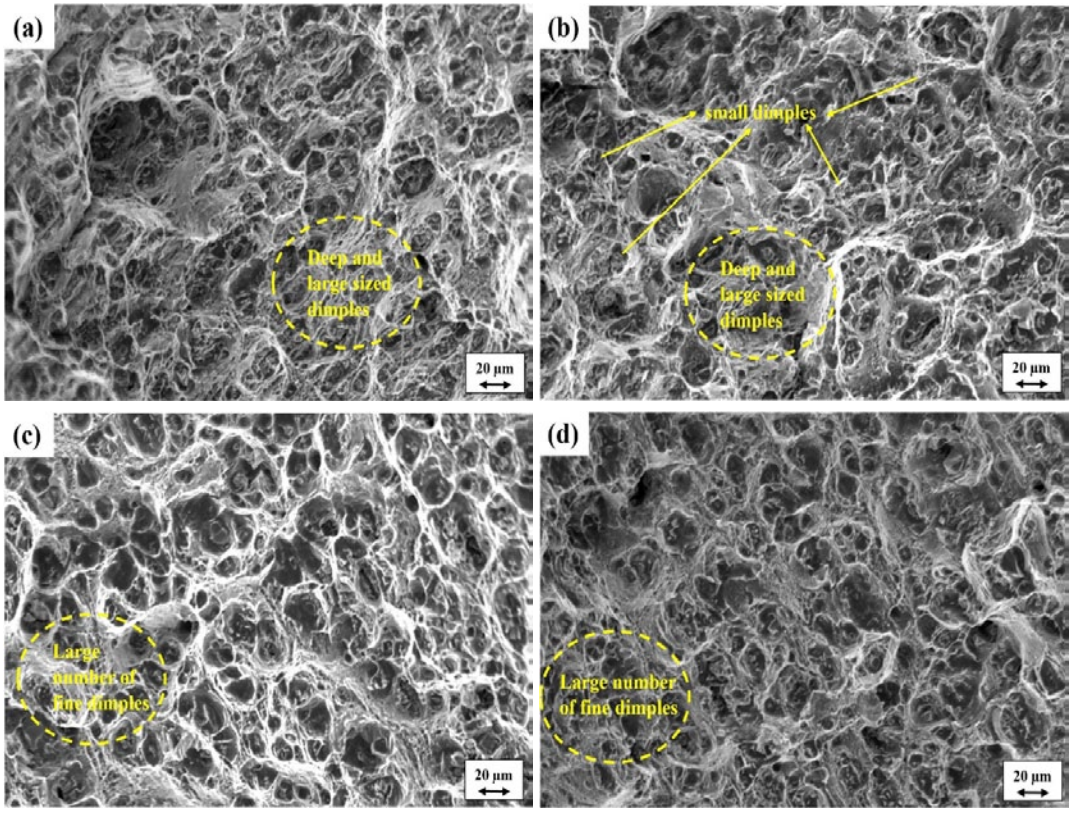

Fig. 12. Fractographies of the Impact test samples: (a) S_1, (b) S_2, (c)S_3, (d) S_4

parison with BM. The incorporation of rGO particles improved the conductivity behavior of FSPed specimens. This finding highlights the formation of conducting channels by rGO particles, which leads to heat transfer. Using rGO particles, FSPed composites had a comparable increase in thermal conductivity. Compared to rGO-reinforced specimens, adding reinforcements like MWCNT significantly improves thermal conductivity. This may be because of the increased friction and plasticization lead to the development of highly conductive rGO at lower oxygen levels. As the time interval increases, the thermal conductivity of every specimen exhibits an increasing pattern. This corresponds to the enhanced mobility of heat carriers. It illustrates the function of FSPed AA7075-T6 rGO-based composites for cylinder liner applications. Suganeswaran et al.'s thermal conductivity research shows that the addition of Al_2O_3 and SiC reinforcements increases thermal conductivity in proportion to voltage increases. Similarly, the incorporation of rGO and MWCNT hybrid reinforcements significantly improved thermal conductivity compared to the base material, AA7075-T6, as a result of carbon particle expansion. As the phonons are the primary carriers of thermal energy in non-metallic solids an assumption was made that they propagate through the lattice as quantized vibrational energy waves. In metals and some semiconductors, free electrons also contribute significantly to thermal conductivity, but they transport thermal energy only by moving through the lattice and transferring energy through collisions. In these experimental results as well, as the thermal conductivity improved for the other samples when compared to the base material, it was assumed that it can be certainly caused by the phonons and electrons caused the increase in thermal conductivity. This growth makes the oxide film less dense, which makes it easier for phonons and electrons to move around. This makes the material more thermally conductive [44].

Fig. 14 displays the CTE of the BM AA7075-T6 and FSPed specimens over a 300-670 K temperature range. The average value of BM was 10.75×10^{-4} K^{-1}. Across the entire temperature range, the FSPed specimen exhibits significantly lower CTE values than the BM (17.6%). The processing phase's residual stress-relieving phenomenon may be responsible for this, while material movement from the advancing side to the retreating side may conceal the BM's pores. This action prevents the AA7075 matrix from expanding during the thermal cycling stage. The inclusion of rGO particulates in the base matrix contributes to a decrease in CTE values compared to the BM and FSPed specimens. This is probably due to the following reasons: (i) confinement of matrix through pinning of reinforcements; (ii) strain mismatch between the BM AA7075-T6 matrix and the reinforcements; (iii) development of effective interfacial bonding; and (iv) decrease in the CTE of rGO particles. The FSPed hybrid reinforcement (rGO + MWCNT) possesses a superior CTE of 33.34% over all the specimens. The addition of the reinforcements along with the grain refinement can create more thermal stresses and leads to dislocation generation. It can indeed cause dislocations in the matrix material due to various

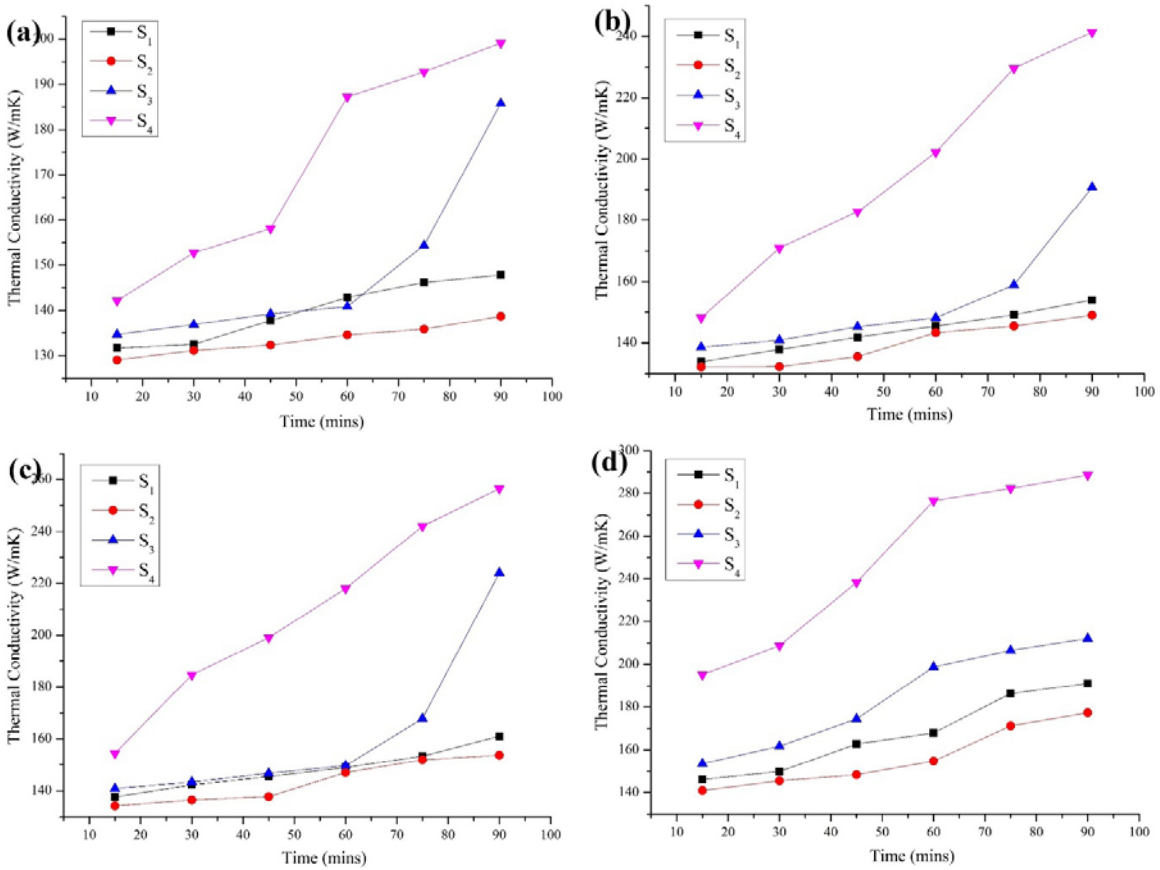

Fig. 13. Thermal conductivity of all specimens: (a) 50 V, (b) 100 V, (c) 150 V, (d) 200 V

mechanisms, including differential thermal expansion, elastic and plastic mismatch, load transfer, interfacial reactions, and localized stress fields. These dislocations can affect the mechanical properties of the composite material, often leading to increased strength and toughness.

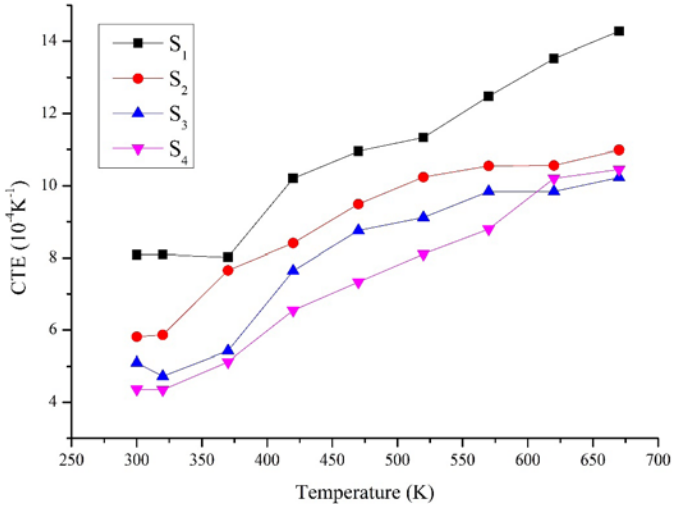

Fig. 14. CTE measurements of all specimens

4.7. Tribological Analysis – Wear Behavior

Fig. 15 represents the wear rate variation of BM AA7075-T6 and FSPed specimens at the sliding distance. All the specimens revealed that the wear rate was initially high due to the adhesive nature of the wear. The FSPed AA7075-T6 had a 21.2% lower wear rate than the BM AA7075-T6. The outcomes of the FSP processing stage are grain refinement and pore closure, which prevent plastic deformation during sliding. The incorporation of rGO particulates decreases the wear rate of FSPed surface composites. Some of the reasons for this are (i) the specimen pin and counter disc have a smaller contact area; (ii) the rGO and MWCNT reinforcement particles are spread out evenly and pin down the Al matrix during the sliding condition; and (iii) the reinforcements stop gaps from getting through to the layer below. The FSPed AA7075-T6 + (rGO + MWCNT) specimen achieved a comparatively greater wear resistance of 19.9% when compared to the FSPed AA7075-T6 + rGO specimen. The stronger hardness and interfacial bond between the BM AA7075-T6 and reinforcement particles keep the reinforcements from coming loose when the part slides, which lowers wear. It also influences the specimen with high thermal conductivity by transmitting heat to the atmosphere more quickly, which limits the amount of plastic deformation. Similar trends were also observed by Kumar et al., where they reinforced industrial waste into the aluminum alloy using the FSP technique, which helped to improve the wear resistance of the SMMCs [45-46].

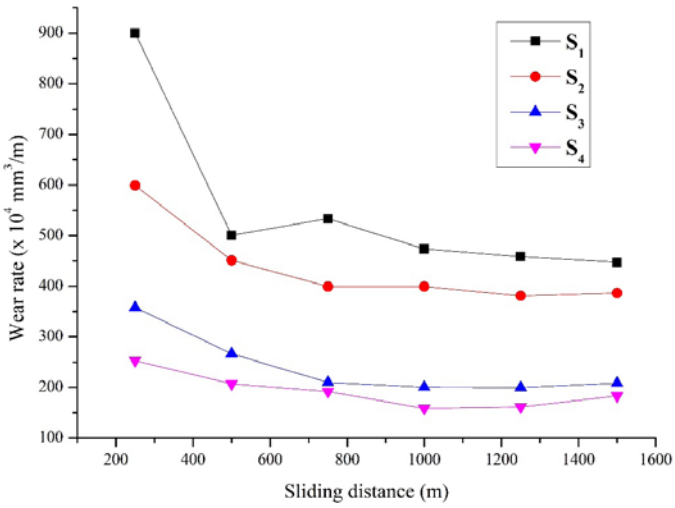

Fig. 15. Wear rate of all specimens

5. Conclusions

Using the FSP technique, the present work successfully fabricated hybrid MMC AA7075-T6 (reinforced with rGO and rGO+MWCNT). We used multipass FSP to break up and spread out the formed clusters evenly and uniformly after making the hybrid MMC, which had layers of rGO and MWCNT nanoparticles. We thoroughly investigated the microstructural features and mechanical properties of mono- and hybrid-reinforced MMC. Below is a summary of the investigation's findings:

(a) The best FSP parameters found using the RSM-based DoE method are RS at 1100 rpm, TS at 50 mm/min, and 2 passes that show the best tensile strength and microhardness. These findings strongly match the experimental findings.

(b) When the right FSP-optimal process parameters are used, strong interfacial bonding between the matrix and reinforcement particles is seen in all MMCs. This means that the morphological properties are better after the reinforcements are added to the metal matrix.

(c) The microstructure of AA7075-T6 + (rGO + MWCNT) showed a significant reduction in grain size due to the dynamic recrystallization and grain refinement.

(d) The AA7075-T6 + (rGO + MWCNT) sample achieves a microhardness of 192 HV, significantly higher than the BM sample. This enhancement is due to the Hall patch relationship and Orowan strengthening mechanisms.

(e) The addition of equal amounts of rGO and MWCNT reinforcement particles to the AA7075-T6 metal matrix led to a 50% increase in impact toughness compared to the base metal. This is due to the strong bond between the reinforcement particles and aluminum.

(f) The thermal conductivity of the (rGO + MWCNT)-reinforced SMMC exhibits a continuous increase from 30-80 W/mK with the variation in voltages tested, which can enhance the SMMC utility as mobile heat carriers.

(g) The wear rate also improved to 1.5 times that of the BM with the addition of (rGO + MWCNT) reinforcements into the SMMC, as the reinforcement particles prevented the pulling-out behavior during sliding and thus reduced the wear rate.

The improvements made to the FSPed hybrid reinforcement specimen lead to better tensile strength, microhardness, impact strength, thermal conductivity, and wear rate. This increases the likelihood of producing surface-reinforced hybrid MMCs for various engineering applications.

Future Scope

Surface-reinforced hybrid MMCs produced via FSP hold tremendous promise for future applications. By carefully managing the process parameters, FSP makes it possible to make MMCs with specific mechanical properties, such as higher strength, resistance to wear, and thermal stability. This makes them perfect for high-performance uses in aerospace, automotive, and structures. Additionally, the versatility of FSP allows for the incorporation of lightweight reinforcements and sustainable materials, aligning with the demands of fuel efficiency and environmental sustainability. Furthermore, the ability to customize MMCs for specific functional requirements positions FSP as a key technology for addressing diverse engineering challenges. Overall, FSP-based MMCs represent a transformative approach to materials engineering, offering advanced solutions for next-generation industries while promoting sustainability and performance excellence.

REFERENCES

[1] M.Y. Khalid, R. Umer, K.A. Khan, Results Eng. (2023). DOI: https://doi.org/10.1016/j.rineng.2023.101372

[2] B.S. Sowrabh, B.M. Gurumurthy, Y.M. Shivaprakash, S.S. Sharma, Manuf. Rev. (8), 31 (2021). DOI: https://doi.org/10.1051/mfreview/2021029

[3] A.H. Khan, S.A. Shah, F. Umar, U. Noor, R.M. Gul, K. Giasin, M. Aamir, Mater. **15** (15), 5303 (2022). DOI: https://doi.org/10.3390/ma15155303

[4] A. Sharma, S. Singh, K. Pal, Ceram. Int. **48** (23), 35708-35718 (2022). DOI: https://doi.org/10.1016/j.ceramint.2022.06.212

[5] N.A. Patil, S.R. Pedapati, R.V. Marode, Lubricants **10** (10), 267 (2022). DOI: https://doi.org/10.3390/lubricants10100267

[6] J. Iwaszko, M. Sajed, J. Compos. Sci. **5** (12), 323 (2021). DOI: https://doi.org/10.3390/jcs5120323

[7] Z.Y. Ma, Metall. Mater. Trans. A. **39**, 642-658 (2008). DOI: https://doi.org/10.1007/s11661-007-9459-0

[8] V. Sharma, U. Prakash, B.M. Kumar, J. Mater. Process. Technol. **224**, 117-134 (2015). DOI: https://doi.org/10.1016/j.jmatprotec.2015.04.019

[9] K. Li, X. Liu, Y. Zhao, Coatings **9** (2), 129 (2019). DOI: https://doi.org/10.3390/coatings9020129

[10] S.C. Kundurti, A. Sharma, Arch. Metall. Mater. Friction-Assisted Additive Manufacturing (FAAM) for Multistack Aluminum AA6061-T6/ AA7075-T6 Armor Plates: Numerical Investigation, Fabrication, and Characterization. (accepted) AMM-00153-2023-02.

[11] K. Suganeswaran, S. Ragu Nathan, R. Parameshwaran, N. Nithyavathy, N.R. Dhineshbabu, J. Mater. Eng. Perform. **32**, 3617-3632 (2023). DOI: https://doi.org/10.1007/s11665-022-07354-7

[12] V.K. Jain, P.M. Muhammed, S. Muthukumaran, S.K. Babu, Trans. Indian Inst. Met. **71**, 1519-1529 (2018). DOI: http://dx.doi.org/10.1007/s12666-018-1287-y

[13] L. Pan, C.T. Kwok, K.H. Lo, Surf. Coat. Technol. **357**, 339-347 (2019). DOI: https://doi.org/10.1016/j.surfcoat.2018.10.023

[14] M. Amra, K. Ranjbar, S.A. Hosseini, Trans. Nonferrous Met. Soc. China. **28** (5), 866-878 (2018). DOI: https://doi.org/10.1016/S1003-6326(18)64720-X

[15] L. Chen, Y. Qi, Y. Fei, Z. Du, Met. Mater. Int. **27**, 4263-4270 (2021). DOI: https://doi.org/10.1007/s12540-020-00803-9

[16] O.M. Awad, M.M. Seleman, M.M. Ahmed, H.R. Ammar, J. Pet. Min. Eng. **20** (1), 101-110 (2018). DOI: https://doi.org/10.21608/jpme.2018.40652

[17] E.R. Mahmoud, M. Takahashi, T. Shibayanagi, K. Ikeuchi, Wear **268** (9-10), 1111-1121 (2010). DOI: https://doi.org/10.1016/j.wear.2010.01.005

[18] E.R. Mahmoud, M. Takahashi, T. Shibayanagi, K. Ikeuchi, Mater. Trans. **50** (7), 1824-1831 (2009). DOI: https://doi.org/10.2320/matertrans.M2009092

[19] S.C. Kundurti, A. Sharma, P. Tambe, A. Kumar, Mater. Today: Proc. **56** (3), 1468-1477 (2022). DOI: https://doi.org/10.1016/j.matpr.2021.12.337

[20] N.A. Patil, S.R. Pedapati, O.B. Mamat, Arch. Metall. Mater. **65** (1), 441-457 (2020). DOI: http://dx.doi.org/10.24425/amm.2020.131747

[21] N.A. Patil, S.R. Pedapati, O.B. Mamat, A.M. Hidayat Syah Lubis, Coatings. **10** (6), 541 (2020). DOI: https://doi.org/10.3390/coatings10060541

[22] S.C. Kundurti, V.S. Aditya Mocherla, A. Sharma, R.S. Buradagunta, S. Goel, J. Mines Met. Fuels. **71** (9), 1271-1285 (2023). DOI: https://doi.org/10.18311/jmmf/2023/35454

[23] S. Thanikodi, A.S. Britto, V.S. Dattu, S. Al Obaid, S. Alfarraj, M.A. Kalam, Int. J. Adv. Manuf. Technol. (2023). DOI: https://doi.org/10.1007/s00170-023-12198-z

[24] N.D. Ghetiya, S. Bharti, K.M. Patel, S. Kumar, S.S. Rahimian Koloor, Comp. Adv. Mater. **32**, (2023). DOI: https://doi.org/10.1177/26349833231186162

[25] S. Bharti, N.D. Ghetiya, K.M. Patel, Mater. Today: Proc. **78** (3), 420-425 (2023). DOI: https://doi.org/10.1016/j.matpr.2022.10.182

[26] L. Talarico, S. Pepi, S. Susino, G. Leone, C. Bonechi, M. Consumi, I. Clemente, A. Magnani, Molecules. **28** (15), 5747 (2023). DOI: https://doi.org/10.3390/molecules28155747

[27] P. Rezaei, H.R. Moheghi, A. Amiri Delouei, Water. **15** (8), 1458 (2023). DOI: https://doi.org/10.3390/w15081458

[28] R.J. Pereira, F.A. de Almeida, G.F. Gomes, InStructures. **55**, 1710-1731 (2023). DOI: https://doi.org/10.1016/j.istruc.2023.06.136

[29] K. Raman, V.S. Kumar, J. Adhes. Sci. Technol. 1-27 (2023). DOI: https://doi.org/10.1080/01694243.2023.2270168

[30] A.A. Aafaq, H.S. Jailani, Arab. J. Sci. Eng. **48**, 3647-3664 (2023). DOI: https://doi.org/10.1007/s13369-022-07247-w

[31] A. Kumar, V. Kumar, J. Alloys. Metall. Syst. **3**, (2023). DOI: https://doi.org/10.1016/j.jalmes.2023.100022
[32] R.H. Myers, D.C. Montgomery, C.M. Anderson-Cook, John Wiley & Sons, U.S. (2016).
[33] M.Y. Noordin, V.C. Venkatesh, S. Sharif, S. Elting, A. Abdullah, J. Mater. Process. Technol. **145** (1), 46-58 (2004). DOI: https://doi.org/10.1016/S0924-0136(03)00861-6
[34] A. Nooraziah, V.J. Tiagrajah, Appl. Mech. Mater. **666** (2014). DOI: https://doi.org/10.4028/www.scientific.net/AMM.666.235
[35] G. Rajan, S. Mula, J. Manuf. Process. **106**, 19-34 (2023). DOI: https://doi.org/10.1016/j.jmapro.2023.09.073
[36] S.C. Kundurti, A. Sharma, Mater. Res. **26**, (2023). DOI: https://doi.org/10.1590/1980-5373-MR-2023-0176
[37] B.S. Chittoriya, A. Jayant, R. Kumar, Silicon. **15**, 7927-7941 (2023). DOI: https://doi.org/10.1007/s12633-023-02635-9
[38] R. Zhu, Y. Sun, J. Feng, W. Gong, Y. Li, J. Mater. Res. Technol. **27**, 2695-2708 (2023). DOI: https://doi.org/10.1016/j.jmrt.2023.10.123
[39] N. Yuvaraj, S. Aravindan, J. Mater. Res. Technol. **4** (4), 398-410 (2015). DOI: https://doi.org/10.1016/j.jmrt.2015.02.006
[40] R. Butola, Q. Murtaza, R.M. Singari, Surf. Topogr. Metrol. Prop. **8**, (2020). DOI: https://doi.org/10.1088/2051-672X/ab96db
[41] S. Ahmadifard, N. Shahin, M. Vakili-Azghandi, S. Kazemi, Int. J. Adv. Manuf. Tech. **118**, 2205-2220 (2022). DOI: https://doi.org/10.1007/s00170-021-07997-1
[42] Y.S. Sato, M. Urata, H. Kokawa, K. Ikeda, Mater. Sci. Eng. A. **354** (1-2), 298-305 (2003). DOI: https://doi.org/10.1016/S0921-5093(03)00008-x
[43] H. Patle, P. Mahendiran, B.R. Sunil, R. Dumpala, Mater. Res. Express. **6**, (2019). DOI: https://doi.org/10.1088/2053-1591/ab1ff4
[44] K. Suganeswaran, R. Parameshwaran, P. Thangavel, N. Nithyavathy, T. Sivasakthivel, Mater. Res. Express. **6**, (2019). DOI: https://doi.org/10.1088/2053-1591/ab47e3
[45] H. Kumar, R. Prasad, P. Kumar, S.P. Tewari, J.K. Singh, J. Alloys Compd. **831**, 154832 (2020). DOI: https://doi.org/10.1016/j.jallcom.2020.154832
[46] S.R. Nathan, K. Suganeswaran, S. Kumar, P. Thangavel, V.K. Gobinath, J. Manuf. Process. **90**, 139-150 (2023). DOI: https://doi.org/10.1016/j.jmapro.2023.01.084